Transverse electric-thermal-fluid instabilities in an electromagnetic heat exchanger

A.A. Mohekar [a], B.S. Tilley [a,b,*], V.V. Yakovlev [b]

[a] *Department of Mechanical Engineering, Worcester Polytechnic Institute, Worcester, MA 01609, USA*
[b] *Center for Industrial Mathematics and Statistics, Department of Mathematical Sciences, Worcester Polytechnic Institute, Worcester, MA 01609, USA*

ARTICLE INFO

ABSTRACT

Electromagnetic (EM) heat exchangers (HX) are critical components in power beaming applications where EM waves are radiated towards an EM HX, which then converts incident energy into heat or mechanical work. An EM HX consists of a lossy ceramic and a fluid flow that maintains thermal contact with and transfers heat from the ceramic. These materials have loss factors which increase with temperature, so that beyond a critical temperature thermal runaway can take place. Stable characteristic temperatures, which depend on the rate of energy removal from the system, during high-power EM heating of ceramic materials suggest that coolants would be in the gaseous phase. As a first step, we consider a model EM HX system consisting of a horizontal channel containing a viscous, dielectric fluid with a constant coefficient of thermal expansion, bounded from below by a grounded ceramic receiver of finite thickness. The system is subject to plane EM waves, propagating normally to the channel from above, and polarized in the same direction as a plane Poiseuille flow of the coolant. With the Boussinesq approximation, we calculate the base state solution of the system and then investigate the linear stability of this base-state. We find three modes of instability: thermal runaway, Rayleigh-Bénard convection, and a novel instability which we call the *fringe-field instability*, that takes place in the plane normal to base-state flow direction.

1. Introduction

Electromagnetic (EM) heating has been used for decades in thermal food applications [1], chemical processes [2], materials processing [3], and a range of industrial heating applications [4]. The motivation for this work is an electromagnetic heat exchanger (EM HX) which converts electromagnetic radiation to internal energy, and then this internal energy is transferred to a coolant. These devices are being considered in energy collection applications [5] and possibly a way to harness beamed energy [6–9].

A phenomenon which is potentially valuable in this application is *thermal runaway*. In many EM lossy ceramic materials, such as zirconia or silicon carbide, the loss factor of the material increases with increasing temperature. At sufficiently high temperatures and sufficiently large applied electric field strengths, the average temperature in the medium can increase uncontrollably [10]. While this phenomenon leads to significant destruction of the absorbing material, were this power able to be transferred at a sufficiently high rate to a coolant, a potentially large source of energy with a

minimum marginal applied power increase would be beneficial in a variety of applications.

For a slab of a pure material whose loss factor increases with temperature, there are two stable thermal states [11–13] when the wavelength of the applied field is much longer than the slab thickness. At temperatures below a critical temperature, the rate of energy absorbed by the material is balanced by the rate of heat loss to the environment. However, when the temperature increases beyond a critical value, the resulting stable temperature state is much larger. The much higher temperature results in a significant increase in the loss factor of the material, which implies that the field amplitude dissipates over a small region near the slab boundary as it propagates into the slab due to the skin effect. Since this energy absorption takes place over this small region, the rate of energy absorption is small, and again is able to be dissipated through radiation or advection effects outside of the slab.

A potential third stable thermal state is possible when one investigates the electromagnetic-thermal problem of symmetrically applied plane waves, propagating normally through a system of three slabs. The first and third slabs are lossless, while the central slab has a temperature-dependent loss factor [14–16]. With slab thicknesses tuned to fractions of the wavelength of the applied radiation in the given material, a Fabry-Bragg resonance oc-
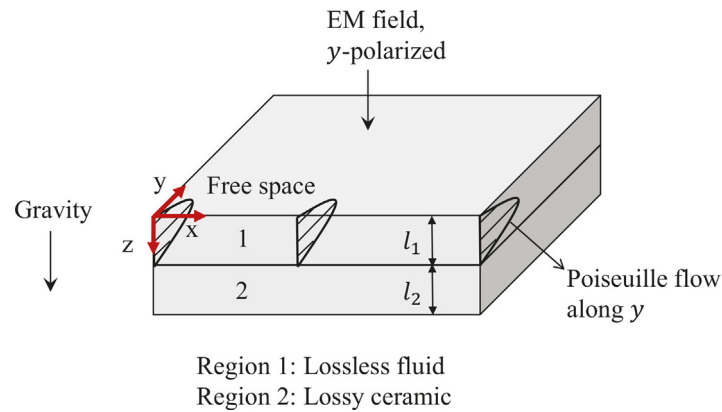
Fig. 1. Geometry of the layered system subjected to EM heating. Layer 1 is lossless fluid and layer 2 is a lossy dielectric. Plane Poiseuille flow is oriented along the *y*-direction.

curs within the ceramic. If the ceramic were lossless, then the amplitude in this phase would be unbounded. However, the loss factor in this region results in a bounded field amplitude within the ceramic, and the resulting absorbed power in the ceramic is dissipated either through radiation or advection from the exterior of the external slabs. The average temperature of this state is intermediate to the two equivalent states from the single-slab case: for materials like silicon carbide or zirconia, the average temperature is on the order of 1000 K, well below any temperature where structural material changes take place. This phenomena is also found in two-layer lossless-lossy systems where the field propagates normal to the lossless layer and the lossy-free space boundary of the ceramic is grounded [17]. This stable branch is attractive for energy harnessing, since the required power needed to maintain the temperature is typically much lower than the two states found for a single-phase slab.

The operating temperatures of this state suggest that any coolant used to harness energy from a laminar system used in an EM HX will be in a gaseous phase. Our concern here is that the development of convection rolls within the coolant may increase the rate of energy dissipation from a lossy slab to effectively quench the temperature of the nonlinear intermediate state, significantly reducing the effectiveness of the device. Other compressible gas phenomena are likely to take place [18], and a comprehensive investigation of all of these phenomena is beyond the scope of a single paper. In this work, we focus on the potential convection instability mechanisms which can arise due to the fluid-thermal-electromagnetic interaction in these systems, and hence consider coolants which are Boussinesq fluids: viscous, incompressible fluids where the temperature dependence of the density is included only in the momentum equation corresponding to the fluid component in the direction of gravity.

To better quantify the mechanisms, we consider a canonical situation shown in Fig. 1. Consider a horizontal fluid channel, thickness l_1, below which is a slab of thickness l_2. The Boussinesq fluid flows through the channel in the *y*-direction, and a plane-wave electric field, polarized in the *y*-direction and propagating in the *z*-direction normal to the system. The fluid is electrically lossless, and the EM wave is partially absorbed by the ceramic, with the absorbed energy converted to internal energy within the slab.

When the fluid in the region 1 is stationary and heated from below due to the perfect thermal contact with the slab, the stability of this base state is similar to the classical rigid-rigid Rayleigh-Bénard (RB) convection problem [19]: the onset of convection takes place when the Rayleigh number, the ratio of buoyancy and viscous stresses within the fluid layer, is greater than some critical value. The difference between our problem and the classical RB convection is that the applied temperature difference across the fluid channel is nonlinearly related to the applied electric field am-

plitude. We note in this isotropic case that the axes of the developing parallel convection rolls align in any direction in the *xy*-plane. From early experiments on RB convection [19], it is known that the Nusselt number, which is a measure of convective heat transfer within the fluid, improves with Rayleigh number. In addition, many geometrical parameters such as inclination angle [20], boundary roughness [21,22], affect the heat transfer characteristics between the ceramic and the fluid region. In our EM HX, we expect to see improvements in the convective heat transfer as the applied EM power increases (since Rayleigh number increases), which would quench the thermal runaway and affect the performance of the device, but this analysis requires full 3D numerical simulation of the RB convection coupled to EM heating for the ceramic. Moreover, it may be possible to extend Howle's approach [23,24] and design an active controller to alter RB convection characteristics so that performance of the EM HX may be optimized. As a first step towards these considerations, this paper is focused on identifying different primary instability mechanisms within the EM HX.

When there is a laminar flow, then the stability problem is more complicated. Gage and Reid [25] note for the classical problem of a plane Poiseuille flow base-state in a horizontal channel, heated from below with a linear temperature profile in the fluid, that the primary instability to this flow is to convection rolls in the transverse plane (i.e., the convection roll axes are in the same direction as the base-state flow direction). The classical Tollmien-Schlichting instability follows Squire's Theorem [26] for the case when the fluid is stably stratified (i.e., density increases in the direction of gravity). We restrict our study to the case when the primary instability is due to the onset of convection rolls, whose axes are aligned in the *y*-direction and amplitude varies in the *xz*-plane.

Onset of RB convection in a stationary absorbing fluid layer undergoing heating due to one sided irradiation by plane EM waves is considered by Gilchrist and Kriegsmann in [27]. Their model assumes a constant dielectric loss factor of the fluid layer and onset of convection is due to nonuniform EM heating of the fluid layer. This model is extended considering plane wave irradiation from both sides of the fluid layer by Bhattacharya and Basak in [28] considering water as the fluid, and in [29] with oil as the fluid region. A common theme between these models is the constant dielectric loss factor of fluids, and onset of convection is due to nonlinear density gradients in the fluid layer that occur due to EM heating of the fluid itself. The difference between our model and previous works is that we consider a lossless Boussinesq fluid which is heated from below as a result of heat generation in the lossy layer. Since the loss factor is temperature-dependent in the ceramic region, the temperature and electric field perturbations are coupled to each other. We later show that this coupling gives rise to a novel primary instability which we call it as *fringe-field instability*.

Section 2 presents the full system of partial differential equations for this system, and perform a nondimensionalization. Section 3 describes the computational methods to find the base-state solution of this system, since the thermal-electric problem depends nonlinearly on temperature and electric field amplitude. In Section 4, we formulate the linear stability problem. In Section 5, we present our results for the instabilities due to thermal runaway, Rayleigh-Bénard convection, along with this new fringe-field instability. We conclude our paper in Section 6.

2. Governing equations

Our focus is understanding the fluid-thermal-electric field interactions which can lead to instabilities of an electromagnetic heat exchanger near the Fabry-Bragg resonance. In order to achieve this electric field resonance, where the double S-curve is possible, the following conditions need to be satisfied [17]

$$l_1 = \frac{n_1 \lambda_1}{4} \text{ and } l_2 = \frac{n_2 \lambda_2}{2}, \tag{1}$$

where n_1 and n_2 can be any odd number, i.e., $1, 3, 5, \ldots$, λ_1 and λ_2 are wavelengths in regions 1 and 2, respectively. Until otherwise noted, we take $n_1 = 3$ and $n_2 = 1$. For later confirmation of our results, we restrict the carrier frequency to be 2.45 GHz.

We introduce nondimensional variables as

$$\vec{x} = \frac{\vec{x}'}{l_1}, \vec{u} = \frac{\vec{u}' l_1}{\alpha_1}, t = \frac{t' \alpha_1}{l_1^2}, p = \frac{p' l_1^2}{\mu \alpha_1},$$

$$\vec{E}_j = \frac{\vec{E}'_j}{E_0}, T_j = \frac{T'_j - T_A}{T_A}, k_0 = k'_0 l_1,$$

where primed quantities represent respective dimensional variables, $\vec{x}$ is the position vector with components (x, y, z), l_1 is the thickness of region 1, $\vec{u}$ is the fluid velocity vector which has components (u, v, w) in x, y, and z directions, respectively, $\alpha_1 = \frac{k_1}{\rho_1 c_{p_1}}$ is the fluid thermal diffusivity, k_1 is the fluid thermal conductivity, ρ_1 is the fluid density, c_{p_1} is the fluid specific heat, p is the fluid gauge pressure, μ is the fluid dynamic viscosity. Further, $\vec{E}_j$ is the electric field vector with components (E_{jx}, E_{jy}, E_{jz}), where the subscript j represents the material region (i.e., $j = 1$ represents the fluid region, while $j = 2$ represents the ceramic region), E_0 is the intensity of incident electric field, T_j is the temperature, T_A is the ambient temperature, k_0 is the wavenumber of EM waves in free space. Note that our choice of the thermal conduction time-scale is classical (see Drazin and Reid [19]), but as we shall see below, the base-state solution needs to be solved computationally, as the temperature difference across the fluid channel depends nonlinearly on the applied electric field strength. Using a free-fall time scale in our problem is not practical.

The dimensionless thermal energy balance for the geometry shown in Fig. 1 can be represented by

$$\frac{\partial T_1}{\partial t} + \vec{u} \cdot \nabla T_1 = \nabla^2 T_1, \ 0 < z < 1, \tag{2a}$$

$$\rho c_p \frac{\partial T_2}{\partial t} = k \nabla^2 T_2 + P |E_2|^2 \epsilon''_2(T_2), \ 1 < z < 1 + l, \tag{2b}$$

where $\rho = \frac{\rho_2}{\rho_1}$, ρ_2 is the ceramic density, $c_p = \frac{c_{p_2}}{c_{p_1}}$, c_{p_2} is the ceramic specific heat, $k = \frac{k_2}{k_1}$, k_2 is the ceramic thermal conductivity, $P = \frac{E_0^2 \omega \epsilon_0 l_1^2}{2 k_1 T_A}$ is the dimensionless power of EM waves, and $l = l_2/l_1$.

Electric field propagation through free space, regions $j = 1$ and 2 is governed by the Maxwell's equations

$$\nabla \cdot \left(\epsilon_j \vec{E}_j \right) = 0, \tag{3a}$$

$$\nabla^2 \vec{E}_j - \nabla \left(\nabla \cdot \vec{E}_j \right) + k_0^2 \epsilon_j \vec{E}_j = 0. \tag{3b}$$

The strength of the electric field depends on the power of incident EM waves. Dielectric constants of free space and region 1 are assumed to be constant, and electric fields in free space and region 1 become divergence free. Finally, fluid obeys the Navier-Stokes equations with the Boussinesq approximation [30]

$$\nabla \cdot \vec{u} = 0, \tag{4a}$$

$$\frac{1}{Pr} \left[\frac{\partial \vec{u}}{\partial t} + (\vec{u} \cdot \nabla) \vec{u} \right] = -\nabla p + \nabla^2 \vec{u} - Ra T_1 \hat{z}, \tag{4b}$$

where $Pr = \frac{\mu c_{p_1}}{k_1}$ and $Ra = \frac{\rho_1 g l_1^3 \beta T_A}{\mu \alpha_1}$ are Prandtl and Rayleigh numbers, respectively.

At the interface between free-space and region 1 (at $z = 0$), the fluid velocity vanishes by the no-slip boundary condition, thermal losses to the surroundings are characterized by Newton's law of cooling with a constant heat transfer coefficient along with radiation losses, and the tangential electric and magnetic fields are continuous

$$\left. \begin{array}{l} \vec{u} = 0, \frac{\partial T_1}{\partial z} = Bi T_1 + R\left[(T_1 + 1)^4 - 1 \right], \\ \hat{n} \times \nabla \times \vec{E}_a = \hat{n} \times \nabla \times \vec{E}_1, \\ \hat{n} \times \vec{E}_a = \hat{n} \times \vec{E}_1, \end{array} \right\} \text{ at } z = 0, \tag{5}$$

where $Bi = \frac{h l_1}{k_1}$, h is specified heat transfer coefficient, $R = \frac{\xi s_r l_1 T_A^3}{k_1}$ is the radiation parameter, s_r is the Stefan-Boltzmann radiation heat constant, and ξ is the emissivity of the surface at $z = 0$, $l = \frac{l_2}{l_1}$, l_2 is thickness of region 2. Physically, Bi and R characterize the heat lost to the environment through convection and thermal radiation, respectively. As a first-order estimate, we use Nusselt number correlations characterizing natural convection between ambient air and the wall [31], which gives $Bi = 0.4$. Using typical emissivity values for ceramic metals at high temperature [31] we find that $R = 0.02$.

At the interface between regions 1 and 2, the no-slip boundary condition is applied to the fluid velocity, perfect thermal contact is maintained, i.e., heat flux and temperature are continuous, and boundary at $z = l_1 + l_2$ is thermally insulated, and tangential components of the electric and magnetic fields are continuous

$$\left. \begin{array}{l} \vec{u} = 0, T_1 = T_2, \frac{\partial T_1}{\partial z} = k \frac{\partial T_2}{\partial z}, \\ \hat{n} \times \nabla \times \vec{E}_1 = \hat{n} \times \nabla \times \vec{E}_2, \\ \hat{n} \times \vec{E}_1 = \hat{n} \times \vec{E}_2, \end{array} \right\} \text{ at } z = 1, \tag{6}$$

The boundary at $z = l_1 + l_2$ is electrically grounded [32] and thermally insulated as shown in Eq. (7)

$$\hat{n} \times \vec{E}_2 = \mathbf{0}, \frac{\partial T_2}{\partial z} = 0, \text{ at } z = 1 + l . \tag{7}$$

3. Base-state solution

At steady state, it is assumed that convection is absent within the fluid layer. We are looking for solutions independent of the x- and y-directions, and temperature depends on z only. Since ϵ_2 depends only on temperature and incident plane wave is polarized in the y-direction, the electric field vector becomes divergence free (Gauss's law), and Maxwell's Eq. (3b) reduce to the Helmholtz equation.

The plane-wave electric field solution in free space at the steady-state is given by

$$\vec{E}_a^{ss} = \left[e^{ik_0 z} + \Gamma e^{-ik_0 z} \right] \hat{y}, \tag{8}$$

where Γ is the reflection coefficient between free space and fluid region 1, and $\hat{y}$ is unit vector along the y-direction. Electric fields

penetrating and interacting with regions 1 and 2 are given by $\vec{E}_1^{ss} = \left[E_{1_y}^{ss}(z)\right]\hat{y}$ and $\vec{E}_2^{ss} = \left[E_{2_y}^{ss}(z)\right]\hat{y}$, where $E_{1_y}^{ss}$ and $E_{2_y}^{ss}$ satisfy Helmholtz equation as

$$\frac{d^2 E_{1_y}^{ss}}{dz^2} + k_0^2 \epsilon_1' E_{1_y}^{ss} = 0, \tag{9a}$$

$$\frac{d^2 E_{2_y}^{ss}}{dz^2} + k_0^2 \left[\epsilon_2' + i\epsilon_2''(T_2^{ss})\right] E_{2_y}^{ss} = 0, \tag{9b}$$

along with energy Eq. (2)

$$\frac{d^2 T_1^{ss}}{dz^2} = 0, \tag{10a}$$

$$k\frac{d^2 T_2^{ss}}{dz^2} = -P|E_{2_y}^{ss}|^2 \epsilon_2''(T_2^{ss}). \tag{10b}$$

When we apply (8) to the boundary conditions (5)–(7), the dimensionless base-state problem boundary conditions become

$$\left.\begin{array}{l} \vec{u}^{ss} = 0, \quad \dfrac{dT_1^{ss}}{dz} = Bi\, T_1^{ss} + R\left[(T_1^{ss}+1)^4 - 1\right], \\[2mm] \dfrac{dE_{1_y}^{ss}}{dz} + ik_0 E_{1_y}^{ss} = 2ik_0, \end{array}\right\} \quad \text{at } z = 0, \tag{11}$$

$$\left.\begin{array}{l} \vec{u}^{ss} = 0, \quad T_1^{ss} = T_2^{ss}, \quad \dfrac{dT_1^{ss}}{dz} = k\dfrac{dT_2^{ss}}{dz}, \\[2mm] E_{1_y}^{ss} = E_{2_y}^{ss}, \quad \dfrac{dE_{1_y}^{ss}}{dz} = \dfrac{dE_{2_y}^{ss}}{dz}, \end{array}\right\} \quad \text{at } z = 1, \tag{12}$$

$$E_{2_y}^{ss} = 0, \quad \frac{dT_2^{ss}}{\partial z} = 0, \text{ at } z = 1 + l, \tag{13}$$

The system (9)–(13) is nonlinear due to the temperature dependent loss factor of the ceramic region. Approximations to the analytical solution of the above system are presented in [17] using thin-domain asymptotics, where the leading-order temperature is spatially uniform in the limit of small thermal losses to the surroundings. In our problem, consideration of spatial variation of the temperature within the fluid is necessary to find density profiles in the fluid, therefore, we solve (9)–(13) numerically using a second-order central finite difference scheme in conjunction with the Newton-Raphson method to solve the nonlinear algebraic system. We discretize the 1D computational domain with 200 data points in each region, and the computational solution is said to have converged after iterates are within a tolerance of 10^{-4}.

Since convection is absent at the base-state, fluid mass and momentum conservation equations can be solved independently. Under the assumption of fully-developed parallel flow in laminar regime, flow profiles can be described by a plane Poiseuille flow in the y-direction. To get an expression of velocity profiles, we impose a constraint on the base-state flow in terms of dimensionless average velocity

$$Pe = \int_0^1 (\bar{u}^{ss} \cdot \hat{y})\, dz, \tag{14}$$

where $\bar{u}^{ss}$ is the parabolic profile of fluid velocity which is directed in the y-direction, $Pe = \frac{\bar{V}l_1}{\alpha_1}$, where $\bar{V}$ is the dimensional average velocity of the flow. Plane Poiseuille flow, satisfying (14) and no slip boundary conditions, is given by $\bar{u}^{ss} = [PeF(z)]\hat{y}$, where $F(z) = -6(z^2 - z)$. Resolving $\bar{u}^{ss}$ into component form, we get

$$u^{ss}(z) = 0, \quad v^{ss}(z) = Pe\, F(z), \quad w^{ss}(z) = 0. \tag{15}$$

Since the fluid flow profiles at the base state are not affected by temperature, we extend the numerical solution of the base-state
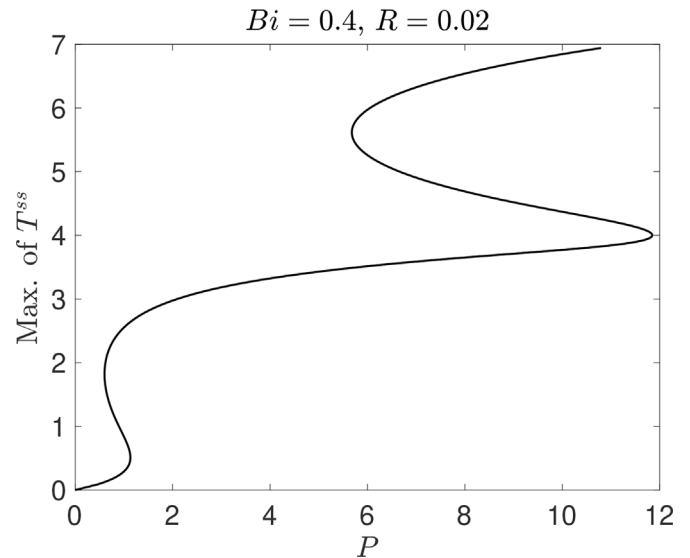
Fig. 2. Double S-curve we get by solving (9), (10) along with the numerical continuation approach.

EM-thermal problem to generate power response curves by using a numerical continuation algorithm. One such power response curve is shown in Fig. 2. We get a double S-curve because channel thicknesses are chosen according to resonance criteria [14,17,33].

Branches of the response curve are shown in Fig. 2, where negative slopes are inherently unstable due to thermal runaway instability [11]. But on the stable sections of the power response curve, RB convection can initiate when buoyancy forces dominate over the viscous stresses within the fluid. Looking at the classical RB convection problem (where a stationary fluid layer is heated from below by a specified temperature gradient at the base state), instability occurs when $\bar{Ra} > \bar{Ra}_{\text{crit}}$, where

$$\bar{Ra} = \frac{\rho_1 g {l_1}^3 \beta T_A \Delta T_1^{ss}}{\mu \alpha_1} = Ra\, \Delta T_1^{ss}, \tag{16}$$

where $\Delta T_1^{ss} = T_1^{ss}(z=1) - T_1^{ss}(z=0)$ is the dimensionless temperature drop across the fluid layer. In our problem, ΔT_1^{ss} increases nonlinearly with applied power (as seen from the response curve Fig. 2), and there are two ways RB instability can be instigated. The first way is to keep Ra constant, and increase the applied power P; since ΔT_1^{ss} increases with increasing P, there is a P_{crit} when $P > P_{\text{crit}}$, convection initiates. The second approach is to keep P constant and convection initiates when $Ra > Ra_{\text{crit}}$, i.e., ΔT_1^{ss} is fixed but importance of buoyancy is increased by manipulating other material properties. In this work, we investigate the later approach.

In order to demonstrate how a base-state power response curve may be useful to determine onset characteristics of the RB convection, in Fig. 3, we plot ΔT_1^{ss} as a function of P when the value of the radiation parameter R is varied. At lower temperatures, convective heat losses dominate, but at higher temperatures radiation losses become more significant since they are proportional to 4th power of temperature [33]. Since we want to understand the impact of thermal losses when EM HX operated on the middle and upper branch, we keep $Bi = 0.4$ and $0 \le R \le 0.02$.

From Fig. 3, we see that when lower branches of these plots are compared as R is varied, ΔT_1^{ss} is slightly smaller for each P compared to $R = 0$. As a first-order estimate we can assume that RB convection initiates at a fixed $\bar{Ra}$, and from (16), we can then say that Ra_{crit} required for the onset of RB convection would be smaller when $R = 0$ (compared to when $R = 0.02$), when the base-state is on the lower branch. Similarly, when the middle and upper
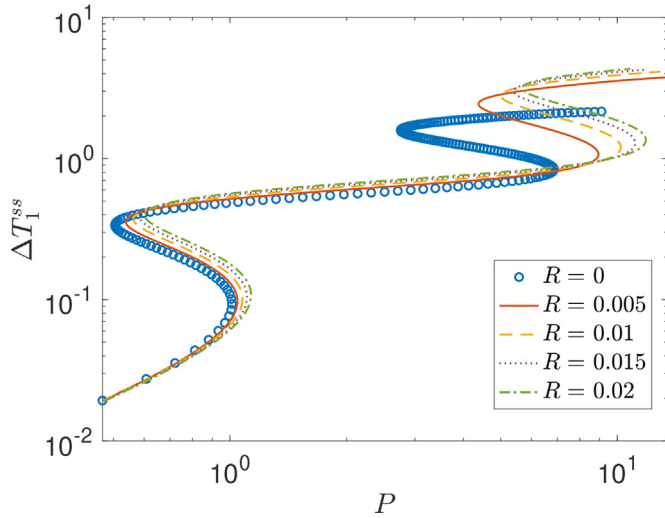
Fig. 3. Temperature drop across the fluid layer from the base-state solution, ΔT_1^{ss}, plotted against the applied EM power. Note that the plot is in logarithmic scale to demonstrate the differences between the curves.

branches are compared, ΔT_1^{ss} are larger as R is varied compared to $R = 0$. We can expect that Ra_{crit} would be smaller at $R = 0.02$ compared to the critical Rayleigh number at $R = 0$. In Section 5.3, we continue this discussion to confirm the above effects.

4. Linear stability theory

The base-state solution lacks convection in the fluid and heat transfer takes place only due to conduction, and our goal here is to find conditions where this solution is unstable to infinitesimal perturbations. We introduce infinitesimal perturbations, and our goal is to determine, through linear stability analysis, whether these disturbances are growing (unstable) or decaying (stable) with time. Perturbations are introduced in the basic solutions as follows

$$\vec{u} = \vec{u}^{ss} + \widetilde{\vec{u}}, \quad p = p^{ss} + \widetilde{p}, \tag{17}$$

$$T_j = T_j^{ss} + \widetilde{T}_j, \quad \vec{E}_j = \vec{E}_j^{ss} + \widetilde{\vec{E}}_j, \tag{18}$$

where the tilde quantities are infinitesimal perturbations. To determine equations governing evolution of these tilde quantities in space and time, we substitute above relations into the system (2)–(7). Since it is assumed that the amplitudes of perturbations are infinitesimal, stability characteristics may be investigated by retaining only the linear terms (and ignoring higher-order terms) with respect to tilde quantities [19]. The primary mode of Bénard instability is when flow direction and wave-vector of perturbations are perpendicular to each other [25]. When plane Poiseuille flow is in the y-direction, (x, z) dependent perturbations represent the dominant mode of instability. Thus, we assume that tilde quantities in the above formulation are y-independent.

Linearizing the Navier-Stokes Eq. (4) yields

$$\frac{\partial \widetilde{u}}{\partial x} + \frac{\partial \widetilde{v}}{\partial y} + \frac{\partial \widetilde{w}}{\partial z} = 0, \tag{19a}$$

$$\frac{1}{Pr}\left[\frac{\partial \widetilde{u}}{\partial t} + PeF(z)\frac{\partial \widetilde{u}}{\partial y}\right] = -\frac{\partial \widetilde{p}}{\partial x} + \nabla^2 \widetilde{u}, \tag{19b}$$

$$\frac{1}{Pr}\left[\frac{\partial \widetilde{v}}{\partial t} + PeF(z)\frac{\partial \widetilde{v}}{\partial y} + \widetilde{w}PeF'(z)\right] = -\frac{\partial \widetilde{p}}{\partial y} + \nabla^2 \widetilde{v}, \tag{19c}$$

$$\frac{1}{Pr}\left[\frac{\partial \widetilde{w}}{\partial t} + PeF(z)\frac{\partial \widetilde{w}}{\partial y}\right] = -\frac{\partial \widetilde{p}}{\partial z} + \nabla^2 \widetilde{w} - Ra\widetilde{T}_1. \tag{19d}$$

Energy Eq. (2) reduce to

$$\frac{\partial \widetilde{T}_1}{\partial t} + PeF(z)\frac{\partial \widetilde{T}_1}{\partial y} + \widetilde{w}\frac{dT_1^{ss}}{dz} = \nabla^2 \widetilde{T}_1 \tag{20a}$$

$$\rho c_p \frac{\partial \widetilde{T}_2}{\partial t} = k\nabla^2 \widetilde{T}_2 \ P|E_2^{ss}|^2 \left(\frac{\partial \epsilon''}{\partial T}\right)_{T_2^{ss}} \widetilde{T}_2 +$$

$$2P\left[\text{Re}(E_{2_y}^{ss})\text{Re}(\widetilde{E}_{2_y}) + \text{Im}(E_{2_y}^{ss})\text{Im}(\widetilde{E}_{2_y})\right]\epsilon''(T_2^{ss}), \tag{20b}$$

The linearized electric field Eq. (3) are given by

$$\nabla \cdot \widetilde{\vec{E}}_a = 0, \tag{21a}$$

$$\nabla^2 \widetilde{\vec{E}}_1 + k_0^2 \widetilde{\vec{E}}_a = 0, \tag{21b}$$

$$\nabla \cdot \widetilde{\vec{E}}_1 = 0, \tag{21c}$$

$$\nabla^2 \widetilde{\vec{E}}_1 + k_0^2 \epsilon_{r_1} \widetilde{\vec{E}}_1 = 0, \tag{21d}$$

$$\nabla \cdot \left(\epsilon_2^{ss}\widetilde{\vec{E}}_2\right) = -\left[\left(\frac{\partial \epsilon_2}{\partial T}\right)_{T_2^{ss}} E_{2_y}^{ss}\right]\frac{\partial \widetilde{T}_2}{\partial y}, \tag{21e}$$

$$\nabla^2 \widetilde{\vec{E}}_2 - \nabla(\nabla \cdot \widetilde{\vec{E}}_2) + k_0^2 \epsilon_2^{ss}\widetilde{\vec{E}}_2 = -\left[k_0^2\left(\frac{\partial \epsilon_2}{\partial T}\right)_{T_2^{ss}} \vec{E}_2^{ss}\right]\widetilde{T}_2. \tag{21f}$$

The linearized boundary conditions (5)–(7) are given by

$$\left.\begin{array}{l} \dfrac{\partial \widetilde{T}_1}{\partial z} = Bi^*\widetilde{T}_1, \\[2mm] \widetilde{\vec{u}} = 0, \\[2mm] \hat{n} \times \nabla \times \widetilde{\vec{E}}_a = \hat{n} \times \nabla \times \widetilde{\vec{E}}_1, \\[2mm] \hat{n} \times \widetilde{\vec{E}}_a = \hat{n} \times \widetilde{\vec{E}}_1, \end{array}\right\} \text{ at } z = 0, \tag{22}$$

$$\left.\begin{array}{l} \dfrac{\partial \widetilde{T}_1}{\partial z} = k\dfrac{\partial \widetilde{T}_2}{\partial z}, \\[2mm] \widetilde{T}_1 = \widetilde{T}_2, \\[2mm] \widetilde{\vec{u}} = 0, \\[2mm] \hat{n} \times \nabla \times \widetilde{\vec{E}}_1 = \hat{n} \times \nabla \times \widetilde{\vec{E}}_2, \\[2mm] \hat{n} \times \widetilde{\vec{E}}_1 = \hat{n} \times \widetilde{\vec{E}}_2, \end{array}\right\} \text{ at } z = 1, \tag{23}$$

$$\left.\begin{array}{l} \dfrac{\partial \widetilde{T}_2}{\partial z} = 0, \\[2mm] \hat{n} \times \widetilde{\vec{E}}_2 = 0, \end{array}\right\} \text{ at } z = 1 + l, \tag{24}$$

where $Bi^* = Bi + 4R[T_{1_{z=0}}^{ss} + 1]^3$.

When ϵ_2 is temperature dependent $\left(\text{i.e., } \frac{\partial \epsilon_2}{\partial T} \neq 0\right)$, the terms with the perturbed ceramic temperature $\widetilde{T}_2$ which appear in (21e) and (21f) are analogous to that of volume charge and current density sources in Maxwell's equations. Let $\frac{q}{\epsilon_0} = -\left[\left(\frac{\partial \epsilon_2}{\partial T}\right)_{T_2^{ss}} E_{2_y}^{ss}\right]\frac{\partial \widetilde{T}_2}{\partial y}$ and $i\omega\mu_0\vec{J} = \left[k_0^2\left(\frac{\partial \epsilon_2}{\partial T}\right)_{T_2^{(0)}} \vec{E}_2^{ss}\right]\widetilde{T}_2$, and then (21e) and (21f) can be written as

$$\nabla \cdot \left(\epsilon_2^{ss}\widetilde{\vec{E}}_2\right) = \frac{q}{\epsilon_0}, \tag{25a}$$

$$\nabla^2 \widetilde{\vec{E}}_2 - \nabla(\nabla \cdot \widetilde{\vec{E}}_2) + k_0^2 \epsilon_2^{ss}\widetilde{\vec{E}}_2 = -i\omega\mu_0\vec{J}, \tag{25b}$$

where q and $\vec{j}$ are playing the role of volume charge and current densities, respectively, in the time-harmonic Maxwell's equations for the electric field $\widetilde{\vec{E}}_2$. These "sources" q and $\vec{j}$ are found in a nonmagnetic medium with a temperature-dependent permittivity, and show how thermal perturbations within the ceramic can induce a fringe field. Moreover, both q and $\vec{j}$ satisfy the time-harmonic charge continuity equation which is given as

$$-i\omega q + \nabla \cdot \vec{j} = 0. \tag{26}$$

With this analogy between (21e) and (21f) and (25), we can, therefore, say that $\widetilde{T}_2$ acts as a source of a perturbed electric (fringe) field (i.e., $\widetilde{\vec{E}}_2$) which originates in region 2 and propagates outwards. In addition, $\widetilde{T}_2$ depends on the y-component of this fringe field $\widetilde{\vec{E}}_2$ as seen in (20b), and the fringe field feeds back into the systems and affects the stability of the system. On the other hand, when ϵ_2 is independent of temperature, regardless of perturbations in temperature, the source terms in linearized Maxwell's equations (21e) and (21f) are absent, and no fringe field is generated.

4.1. Normal-Mode analysis

Since the system (19)–(24) is linear and homogeneous, we can separate the spatial and time dependence of perturbations so that the general solution is a superposition of normal modes in the form

$$\widetilde{\vec{u}} = \vec{u}^{(1)}(z)e^{[i(\vec{a}\cdot\vec{d})+st]} + cc, \quad \widetilde{p} = p^{(1)}(z)e^{[i(\vec{a}\cdot\vec{d})+st]} + cc, \tag{27a}$$

$$\widetilde{T}_j = T_j^{(1)}(z)e^{[i(\vec{a}\cdot\vec{d})+st]} + cc, \quad \widetilde{\mathbf{E}}_j = \mathbf{E}_j^{(1)}(z)e^{i(\vec{a}\cdot\vec{d})+st} + cc, \tag{27b}$$

where $\vec{a} = (a_1, a_2, 0)$ is the wave-vector of perturbations, $\vec{d} = (x, y, 0)$, and s is the growth rate of the perturbations. By representing disturbances as a superposition of normal modes, we determine the stability of the base-state solution by substituting the above forms into the linearized system and then solving for the eigenvalue s for given $\vec{a}$. In general, s is complex valued, which means that growth of disturbances over time can be in the form of traveling waves such that the real part of s, $\text{Re}(s)$, corresponds to exponential variation of amplitudes over time and the imaginary part of s, $\text{Im}(s)$, represents angular speed of the disturbances. When s is real, disturbances exhibit a standing-wave pattern, and their amplitude grows or decays exponentially with time. When $\text{Re}(s) < 0$ for all $\vec{a}$, then amplitudes of disturbances decay over time, and the base-state is linearly stable against infinitesimal disturbances. When $\text{Re}(s) > 0$ for at least one value of $\vec{a}$, then the normal-mode associated with that wavenumber grows exponentially with time, and acts as the dominant mode of instability showing that the base-state solution is unstable. When $\text{Re}(s) = 0$ for a given $\vec{a}$, then the base-state is neither stable nor unstable, but is a neutrally stable state.

With the above formulation, we make the transformations $\frac{\partial}{\partial t} \to s$, $\frac{\partial}{\partial x} \to ia_1$, $\frac{\partial}{\partial y} \to ia_2$, and $\frac{\partial}{\partial z} \to D$. The linearized Navier-Stokes Eq. (19) reduce to

$$ia_1 u^{(1)} + ia_2 v^{(1)} + Dw^{(1)} = 0, \tag{28a}$$

$$\left\{ (D^2 - a^2) - \left[\frac{s}{Pr} + iReF(z)\left(\vec{a}\cdot\hat{u}\right) \right] \right\} u^{(1)} = ia_1 p^{(1)}, \tag{28b}$$

$$\left\{ (D^2 - a^2) - \left[\frac{s}{Pr} + iReF(z)\left(\vec{a}\cdot\hat{u}\right) \right] \right\} v^{(1)}$$
$$= ia_2 p^{(1)} + ReF'(z)w^{(1)}, \tag{28c}$$

$$\left\{ (D^2 - a^2) - \left[\frac{s}{Pr} + iReF(z)\left(\vec{a}\cdot\hat{u}\right) \right] \right\} w^{(1)} - RaT_1^{(1)} = Dp^{(1)}, \tag{28d}$$

where $Re = \frac{Pe}{Pr}$, $\hat{u} = \hat{y}$ is unit vector oriented in the direction of Poiseuille flow of the the base state, and $a^2 = a_1^2 + a_2^2$. Multiplying the x-momentum Eq. (28b) by ia_1 and y-momentum Eq. (28c) by ia_2 and making use of continuity Eq. (28a), we get

$$L_2[Dw^{(1)}] + iReF'(z)(\vec{a}\cdot\hat{u})[w^{(1)}] = a^2 p^{(1)},$$

$$L_2[w^{(1)}] - Ra[T_1^{(1)}] = Dp^{(1)},$$

where $L_2 = \left\{ (D^2 - a^2) - \left[\frac{s}{Pr} + iReF(z)(\vec{a}\cdot\hat{u}) \right] \right\}$.

Analogous to the classical RB problem, we eliminate pressure from the z- momentum Eq. (28d) as

$$\left\{ (D^2 - a^2)^2 + iRe\left(\vec{a}\cdot\hat{u}\right)\left[F''(z) - F(z)(D^2 - a^2)\right] \right\} w^{(1)}$$
$$= \frac{s}{Pr}(D^2 - a^2)w^{(1)} - a^2 RaT_1^{(1)}. \tag{29}$$

The linearized energy Eq. (20) reduce to

$$\left[(D^2 - a^2) - iPeF(z)(\vec{a}\cdot\hat{u}) \right]T_1^{(1)} - w^{(1)}\left(\frac{dT_1^{ss}}{dz} \right) = sT_1^{(1)}, \tag{30a}$$

$$\left[k(D^2 - a^2) + P|E_2^{ss}|^2 \left(\frac{\partial \epsilon''}{\partial T} \right)_{T_2^{ss}} \right]T_2^{(1)} +$$
$$P\left[E_{2_y}^{ss}\left(\vec{E}_2^{*(1)}\cdot\hat{y} \right) + E_{2_y}^{*ss}\left(\vec{E}_2^{(1)}\cdot\hat{y} \right) \right]\epsilon''(T_2^{ss}) = s(\rho c_p)T_2^{(1)}. \tag{30b}$$

Similarly, Maxwell's Eq. (25) are reduced to

$$a_1 E_{a_x}^{(1)} + ia_2 E_{a_y}^{(1)} + DE_{a_z}^{(1)} = 0, \tag{31a}$$

$$\left[(D^2 - a^2) + k_0^2 \right]\vec{E}_a^{(1)} = 0, \tag{31b}$$

$$ia_1 E_{1_x}^{(1)} + ia_2 E_{1_y}^{(1)} + DE_{1_z}^{(1)} = 0, \tag{31c}$$

$$\left[(D^2 - a^2) + k_0^2 \epsilon_{r_1} \right]\vec{E}_1^{(1)} = 0, \tag{31d}$$

$$\frac{d\epsilon_2^{ss}}{dz}E_{2_z}^{(1)} + \epsilon_2^{ss}\left(ia_1 E_{2_x}^{(1)} + ia_2 E_{2_y}^{(1)} + DE_{2_z}^{(1)} \right)$$
$$= -\left[\left(\frac{\partial \epsilon_2}{\partial T} \right)_{T_2^{ss}} E_{2_y}^{ss} \right]ia_2 T_2^{(1)}, \tag{31e}$$

$$\left[(D^2 - a^2 + k_0^2 \epsilon_2^{ss}) \right]\vec{E}_2^{(1)} - \vec{\Psi}\left(ia_1 E_{2_x}^{(1)} + ia_2 E_{2_y}^{(1)} + DE_{2_z}^{(1)} \right)$$
$$= -\left[k_0^2\left(\frac{\partial \epsilon_2}{\partial T} \right)_{T_2^{ss}} \vec{E}_2^{ss} \right]T_2^{(1)}, \tag{31f}$$

where the vector operator $\vec{\Psi} = (ia_1, ia_2, D)$. The perturbed boundary conditions (22)–(24) are given by

$$\left. \begin{array}{l} DT_1^{(1)} = BiT_1^{(1)}, \\ w^{(1)} = Dw^{(1)} = 0, \\ DE_{a_y}^{(1)} - ia_2 E_{a_z}^{(1)} = DE_{1_y}^{(1)} - ia_2 E_{1_z}^{(1)}, \\ DE_{a_x}^{(1)} - ia_1 E_{a_z}^{(1)} = DE_{1_x}^{(1)} - ia_1 E_{1_z}^{(1)}, \\ E_{a_x}^{(1)} = E_{1_x}^{(1)}, \\ E_{a_y}^{(1)} = E_{1_y}^{(1)}, \end{array} \right\} \text{ at } z = 0, \tag{32}$$

$$
\left.\begin{aligned}
&DT_1^{(1)} = kDT_2^{(1)}, \\
&T_1^{(1)} = T_2^{(1)}, \\
&w^{(1)} = Dw^{(1)} = 0, \\
&DE_{1_y}^{(1)} - ia_2 E_{1_z}^{(1)} = DE_{2_y}^{(1)} - ia_2 E_{2_z}^{(1)}, \\
&DE_{1_x}^{(1)} - ia_1 E_{1_z}^{(1)} = DE_{2_x}^{(1)} - ia_1 E_{2_z}^{(1)}, \\
&E_{1_x}^{(1)} = E_{2_x}^{(1)}, \\
&E_{1_y}^{(1)} = E_{2_y}^{(1)},
\end{aligned}\right\} \text{ at } z = 1, \tag{33}
$$

$$
\left.\begin{aligned}
&DT_2^{(1)} = 0, \\
&DE_{2_x}^{(1)} - ia_1 E_{2_z}^{(1)} = 0, \\
&DE_{2_y}^{(1)} - ia_2 E_{2_z}^{(1)} = 0,
\end{aligned}\right\} \text{ at } z = 1 + l. \tag{34}
$$

In addition to conditions (32)–(34), we impose a constraint on the fringe field such that $\vec{E}_a^{(1)}$ is transmitted into the free space, i.e., $\vec{E}_a^{(1)}$ is always propagating from $z = 0$ towards $-\infty$ and nothing is reflected back from $-\infty$ to $z = 0$. The general solution satisfying the constraint and (31b) is

$$
\vec{E}_a^{(1)} = \begin{cases} \vec{c}_a e^{-i\left(\sqrt{k_0^2 - a^2}\right)z}, & \text{for } k_0^2 \geq a^2, \\ \vec{c}_a e^{\left(\sqrt{a^2 - k_0^2}\right)z}, & \text{for } k_0^2 < a^2, \end{cases} \tag{35}
$$

where $\vec{c}_a = (c_{a_x}, c_{a_y}, c_{a_z})$ are unknowns to be determined from (31a) and (32).

Gage and Reid [25] carried out a 3D linear stability analysis on a plane Poiseuille flow heated from below due to a specified adverse temperature gradient across the flow. They found that the primary mode of Bénard instability is when the flow direction and wave-vector of perturbations are perpendicular to each other (i.e., when $\vec{a} \cdot \hat{u} = 0$). When $\vec{a} \cdot \hat{u} = 0$, flow inertia does not affect the stability characteristics as terms containing Re drop out (see (29)). Physically, this means that onset of RB convection in the fluid is a result of competition between buoyancy and shear stresses within the fluid. But when $\vec{a} \cdot \hat{u} \neq 0$, buoyancy must dominate over viscous stresses as well as flow inertia (which is characterized with Re). Therefore, when a Poiseuille flow is in the y-direction, the primary instability leads to convection rolls whose amplitude varies in the xz-plane. In our problem, the plane Poiseuille flow, which is in the y-direction, is heated from below due to heat transfer from electromagnetically heated ceramic. The primary instability occurs when buoyancy dominates over viscous stresses within the fluid, i.e., xz-dependent perturbations are the dominant mode of instability. Thus, from now onward we assume that the wavevector of perturbations is oriented in the x-direction, i.e., $\vec{a} = (a, 0, 0)$.

5. Results

To solve the eigenvalue problem, we approximate spatial derivatives with second-order central difference scheme such that the discretized system of linear equations can be represented as $\mathbf{Mx} = s\mathbf{Rx}$, where $\mathbf{M}$ and $\mathbf{R}$ are square coefficient matrices, and $\mathbf{x}$ is the column vector of unknowns. The eigenvalue problem is solved for given a base-state solution and a using in-built linear algebra package in MATLAB R2021a (using `eigs` function), and the largest real part of eigenvalue then determines stability of the system.

In case of the RB convection instability, we find that all eigenvalues are real-valued, which is expected because the system (29)–(34) is analogous to when flow is initially stationary (i.e., the classical Rayleigh-Bénard problem), and the principle of exchange of instabilities holds [27–29]. Finally, neutral stability curves are generated by utilizing Newton's root finding algorithm which returns base-state solutions that have $\text{Re}\{s\} = 0$ for a given a.

In our problem, there are two possible classical mechanisms that can promote instability–thermal runaway in the ceramic and RB convection in the fluid region. We look at these instabilities individually through a linear stability analysis. This section is therefore organized as follows.

1. We consider the linear stability of the base-state solution when the buoyancy is absent (i.e., $Ra = 0$). This way RB convection is absent, and thermal runaway in the ceramic is the primary instability. We carry out the linear stability analysis to determine which of the base-state solutions are inherently unstable due to the nature of nonlinear EM heating of ceramics. We identify stable and unstable conditions for the base-state solutions using the power response curve framework shown in Fig. 2. As a verification, we compare our results with the finding of Pelesko and Kriegsmann [12] for 1D linear stability analysis. For the 2D scenario, we compare growth rates given by both COMSOL and the linear stability models.

2. Once we identify which states are stable on the power response curve, we then focus on these stable regions and determine Ra_{crit} at which onset of RB instability takes place by carrying out a linear stability analysis.

5.1. Thermal runaway instabilities (No flow and $Ra = 0$)

The temperature response of a ceramic layer during thermal runaway has been studied previously by Kriegsmann in [11]. This work introduced S-shaped power response (or S-) curves that are plots of steady-state temperature as a function of applied EM power. Pelesko and Kriegsmann in [12] considered heating of ceramic laminates and carried out a linear stability analysis, and found out that a branch of a response curve is stable (or unstable) when its slope is positive (or negative). However, their stability analysis is limited to 1D perturbations with zero wavenumber. Since our problem requires consideration of xz-dependent perturbations due to the 2D nature of RB convection, we extend stability analysis done by Pelesko and Kriegsmann [12] to include nonzero wavenumbers.

To verify the linear stability model, we follow the approach in Kriegsmann and Pelesko [12], i.e., we set wavenumber to be zero and solve the eigenvalue problem to determine the growth rate $\text{Re}\{s\}$. In Fig. 4, we mark base-state solutions by red asterisks that have positive values of $\text{Re}\{s\}$, and we arrive at the same conclusion that branches of power response curves with negative (or positive) slope are linearly unstable (or stable) against 1D infinitesimal perturbations. These unstable solutions represent onset of thermal runaway, i.e., any infinitesimal perturbations in the base-state are going to grow exponentially in time resulting in a different state [11]. The direction of the arrows shown in the zoomed portion of the plot in Fig. 4 shows how perturbations evolve with time and stabilize on the middle stable branch. Such exponential transient evolution of T during thermal runaway has been reported in [15,16] and reviewed in the previous section.

5.2. Fringe field instability

Next, we introduce 2D xz-dependent perturbations ($a \neq 0$) and solve for the growth rate for wavenumbers within $0 < a < 2$. We limit the range of wavenumber since growth rates monotonically drop for $a > 2$. If the growth rate is positive at least for one value of wavenumber, we mark the solution to be unstable. The stability characteristics of base-state solutions are shown in Fig. 5. Data points marked by blue squares in Fig. 5(a) are solutions that are stable against 1D perturbations but they become unstable when xz-dependent disturbances are considered. To demonstrate such stability characteristics, we plot the most dangerous growth rate as a function of wavenumber in Fig. 5(b) when 2D perturbations are introduced in the base-state solution at $P = 0.6$ on the middle branch (highlighted by blue squares in Fig. 5(a)). We can see
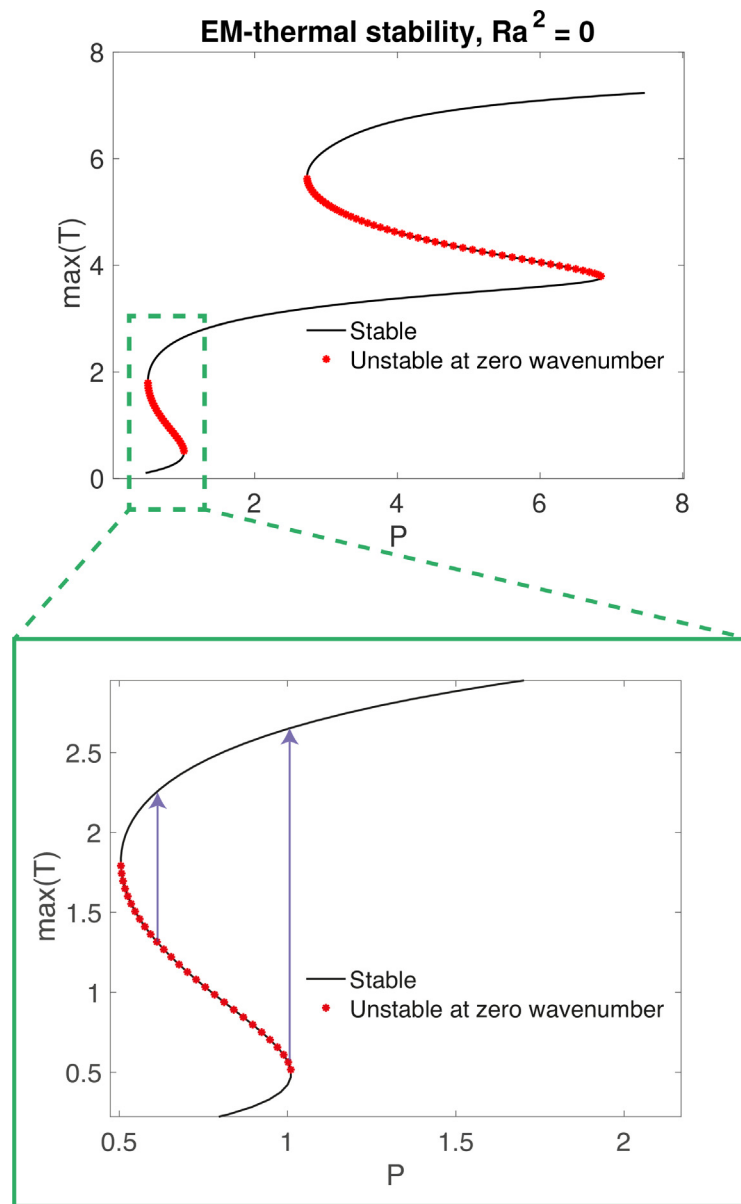
Fig. 4. Stability of solutions on the power response curve against 1D perturbations ($a = 0$); branches with negative slope are unstable which is consistent with [12]. Direction of the arrows in zoomed in portion of the figure indicate that perturbations grow with time and stabilize on the middle stable branch [12].
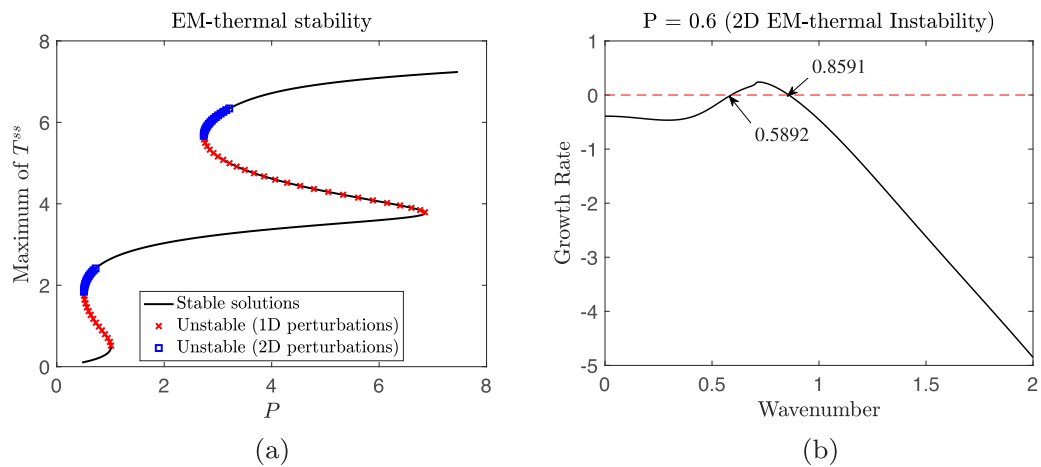
Fig. 5. (a) Stability of solutions on the power response curve against 1D ($a = 0$) and 2D ($a \neq 0$) perturbations; highlighted by blue squares are solutions that are stable when $a = 0$ but unstable at different wavenumbers. (b) Growth rate vs. wavenumber response when $P = 0.6$ on the middle branch (highlighted with blue squares in (a)); it can be seen that this solution is stable at zero wavenumber but becomes unstable against 2D perturbations whose wavenumber is between 0.59 and 0.86. (For interpretation of the references to colour in this figure legend, the reader is referred to the web version of this article.)

that growth rate is positive when wavenumbers are roughly within 0.59 and 0.86. It means that, normal modes whose wavenumber is within this range are going to grow exponentially with time.

To find out how the temperature evolves under the conditions marked by the blue squares in Fig. 5, we carry out direct numerical simulations on a full nonlinear 2D COMSOL model which solves the 2D system of Eqs. (2) and (3) along with boundary conditions (5)-(7) with no fluid flow. To make sure that both linear stability and COMSOL models are consistent, we extract eigenfunctions from the linear stability model and use them in the initial guess setting in the COMSOL simulation (i.e., initial guess in the COMSOL model is $T_{in}(x, z) = T^{ss}(z) + \bar{T}(x, z)$, where $\bar{T}$ is derived from eigenfunction from the linear stability analysis). Since we are after determining transient evolution of $\widetilde{T}$ from the COMSOL model, we define a new variable, $\widetilde{T}$, in the model to store the value of $T(x, z, t) - T^{ss}(z)$ as a function of t. We then take the surface average of $\widetilde{T}$ and plot how the average $\widetilde{T}$ is varying with t in Fig. 6(a). To understand how sinusoidal perturbations are evolving with time, we plot snapshots of T and $|E|$ profiles at different times steps in Fig. 6(b) and (c), respectively. We see that $\widetilde{T}$ keep on growing exponentially until it reaches a new steady-state as seen in Fig. 6(b) and (c) when $t = 500$. These 2D EM-thermal instabilities are a result of the fringe field coupling described by (25) and (26).

To find the mechanisms that promote the fringe-field instability, we explore how environmental heat losses affect the fringe field instability. Since these instabilities are occurring on the middle and upper branches, we increase the radiative heat losses at the boundaries by increasing the radiation parameter R. The stability characteristics from this parametric study are plotted in Fig. 7. We can see that the fringe field instabilities are promoted with environmental heat losses through radiation. To understand the impact of electric field resonance producing double S-curve on the fringe field instabilities we carry out linear stability on the EM-thermal problem by choosing channel thicknesses such that (1) is not satisfied (by keeping $n_1 = 4$ and $n_2 = 1$). In this scenario, we now have a typical S-shaped power response curve at the base-state. Results from the stability analysis are plotted in Fig. 8. We notice that the stability characteristics, even with 2D perturbations, are the same as that of [12]. Fringe field instabilities are absent in case of an S-curve and a branch of an S-curve with negative slope is unstable. This suggests that electric field resonance achieved by satisfying (1) may be one of the driving mechanisms behind the fringe-field instability. This suggests that a separate detailed study is required to identify other factors that may be responsible for the instability mechanism. Future extension of work will be focused on addressing this.

5.3. Rayleigh Bénard instability in the fluid region

First we start with physical explanation of different instabilities that can occur in our problem when there is fluid flow and $Ra \neq 0$.

1. On the stable branches of the response curve (solutions marked by solid lines in Fig. 5(a)) thermal runway and fringe field instabilities are absent, and the primary mechanism of instability is the RB convection which occurs when buoyancy dominates over viscous stresses within the fluid (i.e., when $Ra > Ra_{crit}$ for a given P).
2. Looking at unstable regions marked by red cross and blue square in Fig. 5(a), there are three different primary instabilities that can occur simultaneously (RB convection, thermal runway, and fringe field instabilities), and experimentally we may observe nonlinear interaction between them which would affect the transient growth of perturbations. Linear stability analysis
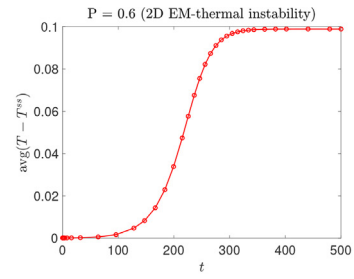
(a) Transient growth of avg($\bar{T}$)
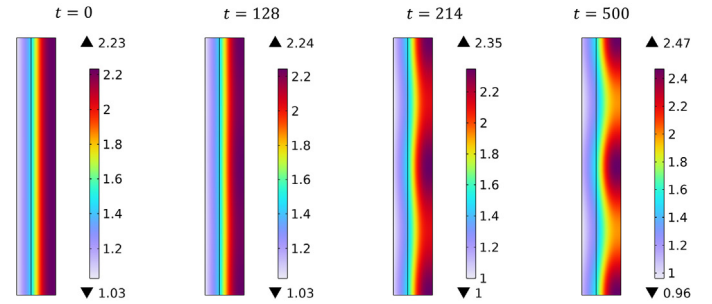
(b) Transient snapshots of 2D T-profiles
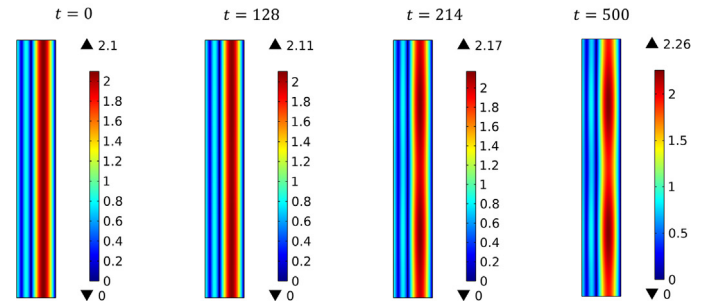
(c) Transient snapshots of 2D $|E|$-profiles

Fig. 6. Direct numerical simulations using COMSOL Multiphysics demonstrating 2D EM-thermal instabilities (also known as fringe field instabilities in this chapter). (a) Transient growth of avg($\widetilde{T}$). (b) Steady-state temperature profile T, and (c) electric-field amplitude profile $|E|$. Note that for (b) and (c), z is the horizontal ordinate and x is the vertical ordinate. The COMSOL model is simulated for $P = 0.6$ and the initial guess is provided such that the model simulates instabilities highlighted by blue square markers in Fig. 5. (For interpretation of the references to colour in this figure legend, the reader is referred to the web version of this article.)

can answer whether a base-state solution is stable or unstable but cannot capture interactions between these instabilities.

To address these points, this subsection is organized in the following way.

1. For a given P on stable branches in Fig. 5, we first generate neutral stability curves that are plots of Ra vs. a when Re$\{s\} = 0$. The smallest value of Ra on these curves is Ra_{crit}, and the wavenumber corresponding to this point is a_{crit}.
2. By utilizing the numerical continuation method discussed earlier in conjunction with the Brent's algorithm (for example
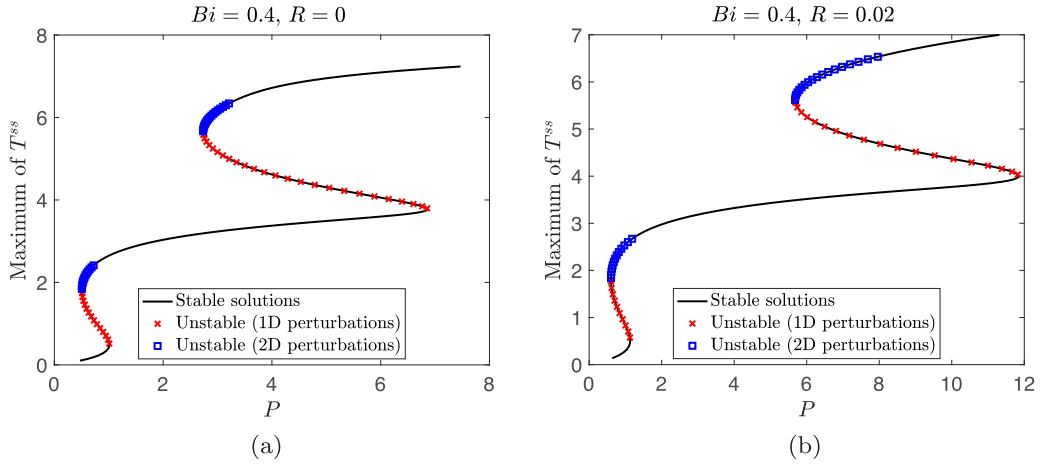
Fig. 7. Impact of the environmental heat losses on the fringe field instability when (a) $R = 0$ and (b) $R = 0.02$. In both of these cases $Bi = 0.4$. Here R is varied as heat loss by thermal radiation is the dominant mode of heat transfer with the environment.
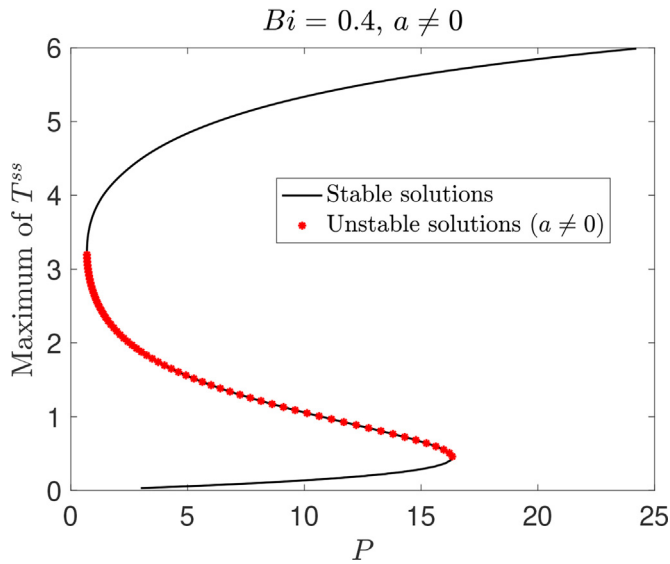
Fig. 8. Stability characteristics of an S-curve. To get this plot, we carry out 2D linear stability analysis on the EM thermal problem, and channel thickness are such that we do not satisfy the resonance criteria (1).
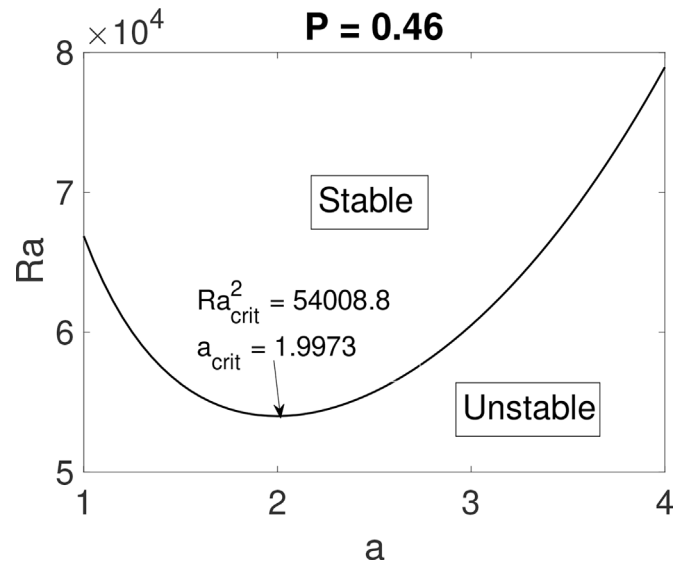
Fig. 9. Neutral curves generated using linear stability analysis in conjunction with a root finding algorithm when incident $P = 0.46$ on the lower stable branch of the response curve shown in Fig. 5(a). Smallest value of Ra on this curve is the Ra_{crit} which determines the onset of RB instability in the fluid region.

[34]), we find out Ra_{crit} as a function of P on stable branches in Fig. 5(a).

To generate neutral stability curves from 2D linear analysis we set $\text{Re}\{s\} = 0$ in (29)–(35), and since the primary instability is to xz-dependent perturbations we have $\vec{a} = (a, 0, 0)$ and $\vec{a} \cdot \hat{u} = 0$. To generate neutral stability curves, we utilize Newton's root finding algorithm with the linear stability code such that for a given a and P, root finder returns a value of Ra such that $\text{Re}\{s\} = 0$. A neutral stability curve is shown in Fig. 9 when applied power of $P = 0.46$ on the lower stable branch in Fig. 5(a). This curve represents the marginal stability state, which means that region above (or below) this curve is unstable (or stable). The lowest value of Ra on this curve gives us Ra_{crit}, i.e., when we have $Ra < Ra_{crit}$, all normal-mode disturbances decay in time, and RB convection is not observed. Critical wavenumber associates with Ra_{crit} is a_{crit} which relates to the wavelength (or size) of the most dominant convection rolls that would be observed experimentally [19]. Such parabolic section of the neutral curve allows us to utilize Brent's algorithm to determine Ra_{crit} (MATLAB's `fminbnd` function in the optimization toolbox). A limiting case of the complete 2D linear stability analy-

sis can be derived by assuming that the linearized heat source is absent, and the equations governing the neutral stability state (29), (30) can be given by,

$$\left(D^2 - a^2\right)^2 w^{(1)} + a^2 Ra T_1^{(1)} = 0, \tag{36a}$$

$$\left(D^2 - a^2\right) T_1^{(1)} - w^{(1)} \left(\frac{dT_1^{ss}}{dz}\right) = 0, \tag{36b}$$

$$\left(D^2 - a^2\right) T_2^{(1)} = 0. \tag{36c}$$

These equations of fluid motion and thermal energy conservation in the fluid region are the same as that of classical RB convection problem and can be solved analytically. To do that (36c) is solved exactly and $T_1^{(1)}$ from (36a) is eliminated using (36b) to get a sixth order ODE in terms of $w^{(1)}$. Physically this problem is analogous to when loss factor of the ceramic is independent of temperature (i.e., $\frac{\partial \epsilon_2''}{\partial T} = 0$ as assumed in [27–29]), and impact of the fringe field is neglected.
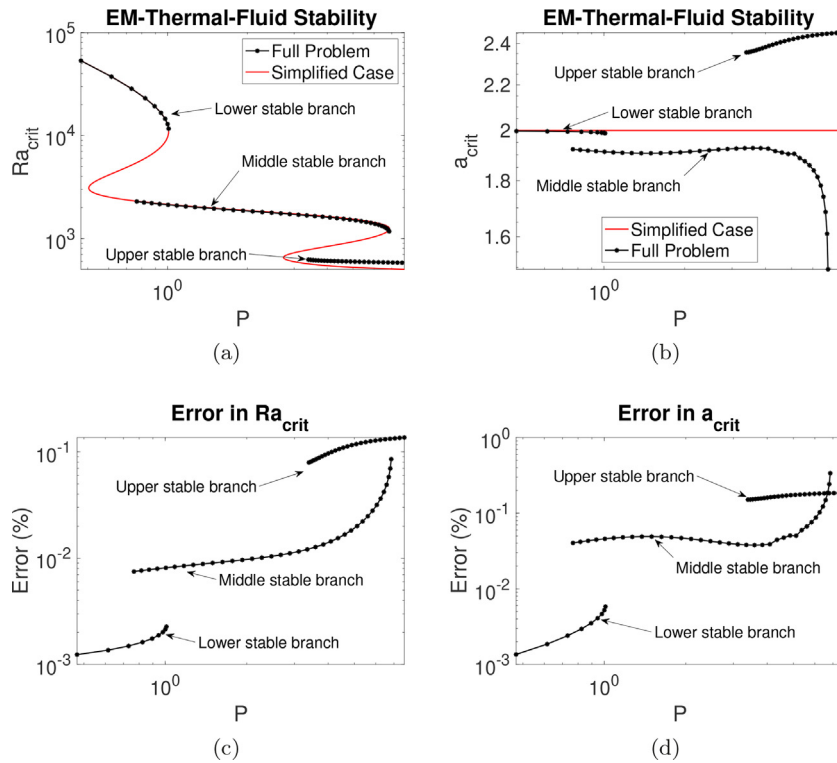
Fig. 10. Comparison between Ra_{crit} and a_{crit} given by the full 2D linear stability analysis and simplified models is shown in (a) and (b), respectively. Relative errors (in %) between the the comparisons shown in (a) and (b) are plotted in (c) and (d), respectively. Here the simplified model does not account for fringe field coupling, maximum values of errors in (c) and (d) are 13.63% and 33.82%, respectively.
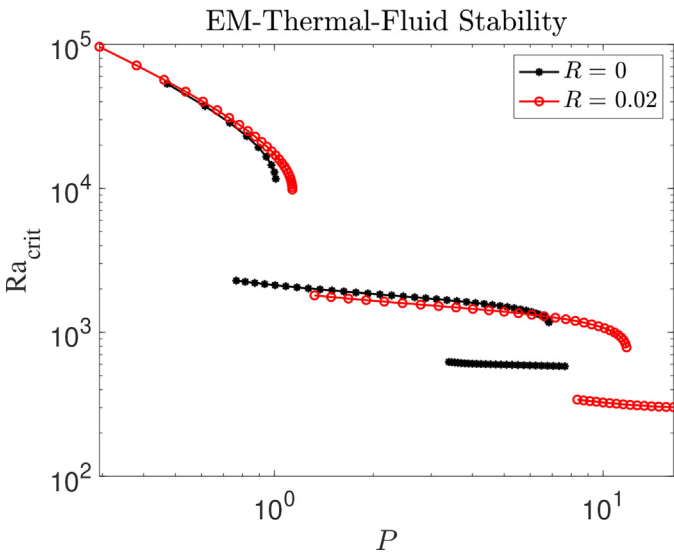
Fig. 11. Impact of radiation heat losses on Ra_{crit}.

In Fig. 10(a) and (b) we show comparison between Ra_{crit} and a_{crit} values given by the full 2D linear stability analysis and the simplified problem given by (36). Relative error between these models is calculated as

$$\text{Error}(\%) = \left| \frac{\text{Full Problem - Simplified Problem}}{\text{Full Problem}} \right| \times 100,$$

and is plotted in Fig. 10(c) and (d). As the simplified model (36) ignores the impact of the fringe field coupling (i.e., coupling between $\widetilde{T}$ and $\widetilde{E}$), errors plots can be a measure of how important the impact of fringe field is. Looking at Fig. 10(c), maximum error in Ra_{crit}

predicted by the simplified model is 13.6%, and is observed on the upper branch. This suggests that the impact of fringe field coupling cannot be ignored when RB convection is expected to take place on the upper branch.

Now we investigate how environmental heat losses affect the onset of RB convection by generating Ra_{crit} vs. P plot with increasing R. This comparison is plotted in Fig. 11. This result confirms our prediction discussed at the end of Section 3. By looking at how ΔT_1^{ss} varies as a function of P, it may be possible to predict how environmental heat losses affect the onset characteristics of the RB convection.

6. Conclusions

In this paper, we have investigated the onset characteristics of natural convection within the fluid. We have considered stability of laminar plane Poiseuille flow of a lossless coolant obeying the Boussinesq approximation in a horizontal channel, situated above a lossy ceramic. Since the fluid is lossless, only the ceramic material undergoes EM heating and the plane Poiseuille flow is heated from below due to the thermal contact with the ceramic layer. It is known that the most dangerous mode of Bénard instability is when flow direction and wave-vector of disturbances are perpendicular to each other [25]. Therefore, through a normal mode linear stability analysis, we determine the critical Rayleigh number, Ra_{crit}, at which the plane Poiseuille flow along the y-direction is unstable to normal modes of disturbances whose wave-vector is parallel to the x-direction. We solve the eigenvalue problem characterizing the stability of the system using a second-order central difference scheme. The model is then validated against an analytical solution which is a limiting case with the constant ceramic loss factor.

In our problem, we have three different primary instability mechanisms that can occur simultaneously: thermal runaway and fringe field instabilities occur within the ceramic and RB convec-

tion instability takes place in the fluid region. Linear stability analysis can tell us whether a base state is stable or unstable, but may not identify which mechanism is causing this instability. To address this we first set $Ra = 0$ (i.e., RB convection is absent) and carry out a 2D linear stability analysis on the EM thermal problem. We found a new fringe-field instabilities that occurs near the leftmost turning point (low power high temperature regions) of the middle and upper branches of the power response curve with nonzero wavenumber. One of the primary mechanisms responsible for this instability is the electric field resonance required for the double S-curve and environmental heat losses. However, further investigation is required to fully explain mechanisms behind the fringe field instability.

The implications from the fringe-field instability mechanism may be significant from practical point of view. We have identified that the most efficient operation of an EM HX may occur on the middle stable branch, especially near the turning point where high ceramic temperature can be maintained at lower applied powers [16]. The 2D fringe field instability described in Fig. 6 lies in the most efficient region of the middle branch. In future work, we can address the research questions on how these instabilities affect the performance of the device. How transients evolve under conditions that are unstable to two or all three instability mechanisms can only be understood through a full 3D computational approach which couples the fluid dynamics and the EM heating of ceramics. We plan to address this in future work.

Declaration of Competing Interest

The authors declare that they have no known competing financial interests or personal relationships that could have appeared to influence the work reported in this paper.

Data availability

Data will be made available on request.

Acknowledgments

References

[1] A.K. Datta, Handbook of Microwave Technology for Food Application, Marcel Decker, Inc., 2001.

[2] N.E. Leadbeater, Microwave Heating as a Tool for Sustainable Chemistry, CRC Press, 2010.

[3] J.A. Aguilar-Garib, Thermal microwave processing of materials, in: S. Grundas (Ed.), Advances in Induction and Microwave Heating of Mineral and Organic Materials, Intech Open: Rijeka, Croatia, 2011, pp. 243–268.

[4] S. Chandrasekaran, S. Ramanathan, T. Basak, Microwave material processing–a review, AIChE J. 58 (2) (2012) 330–363.

[5] A. Jamar, Z. Majid, W. Azmi, M. Norhafana, A. Razak, A review of water heating system for solar energy applications, Int. Commun. Heat Mass Transf. 76 (2016) 178–187.

[6] P. George, R. Beach, Beamed-Energy Propulsion (BEP) Study, Technical report, NASA, NASA/TM-2012-127014, 2012.

[7] P. Kumi, S.A. Martin, V.V. Yakovlev, M.S. Hilario, B.W. Hoff, I.M. Rittersdorf, Electromagnetic-thermal model of a millimeter-wave heat exchanger based on an AlN: Mo susceptor, COMPEL-The Int. J. Comp. Math. Electr. Electron. Eng. 39 (2) (2020) 481–496.

[8] B.W. Hoff, M.S. Hilario, B. Jawdat, A.E. Baros, F.W. Dynys, J.A. Mackey, V.V. Yakovlev, C.E. Andraka, K.M. Armijo, E. Savrun, I.M. Rittersdorf, Millimeter wave interactions with high temperature materials and their applications to power beaming, 52nd IMPI's Microwave Power Symp., Long Beach, CA, 2018, pp. 82–83.

[9] C.M. Hogan, B.W. Hoff, I.M. Rittersdorf, V.V. Yakovlev, Computational characterization of millimeter-wave heat exchangers with an AlN:Mo susceptor of multiple cylindrical elements, J. Microwave Power Electromagn. Energy 56 (1) (2022) 18–36.

[10] M. Chandran, V.B. Neculaes, D. Brisco, S. Katz, J. Schoonover, L. Cretegny, Experimental and numerical studies of microwave power redistribution during thermal runaway, J. Appl. Phys. 114 (20) (2013) 204904.

[11] G.A. Kriegsmann, Thermal runaway in microwave heated ceramics: a one-dimensional model, J. Appl. Phys. 71 (4) (1992) 1960–1966.

[12] J.A. Pelesko, G.A. Kriegsmann, Microwave heating of ceramic laminates, J. Eng. Math. 32 (1) (1997) 1–18.

[13] B.S. Tilley, G.A. Kriegsmann, Microwave-enhanced chemical vapor infiltration: a sharp interface model, J. Eng. Math. 41 (1) (2001) 33–54.

[14] J.M. Gaone, B.S. Tilley, V.V. Yakovlev, Electromagnetic heating control via high-frequency resonance of a triple-layer laminate, J. Eng. Math. 114 (1) (2019) 65–86.

[15] A.A. Mohekar, J.M. Gaone, B.S. Tilley, V.V. Yakovlev, A 2D coupled electromagnetic, thermal and fluid flow model: application to layered microwave heat exchangers, in: IEEE MTT-S International Microwave Symposium, IEEE, (Philadelphia, PA), 2018, pp. 1389–1392.

[16] A.A. Mohekar, B.S. Tilley, V.V. Yakovlev, A triple-layer electromagnetic heat exchanger with plane poiseuille flow: control and local onset of thermal runaway, IEEE J. Multiscale Multiphys. Comput. Tech. 5 (2020) 119–131.

[17] A.A. Mohekar, B.S. Tilley, V.V. Yakovlev, Plane wave irradiation of a layered system: resonance-based control over thermal runaway, in: 17th International Conference on Microwave and High Frequency Heating (AMPERE 2019), Editorial Universitat Politècnica de València, 2019, pp. 292–300.

[18] A.A. Mohekar, B.S. Tilley, V.V. Yakovlev, Resonance, Rayleigh flows and thermal choking: compressible coolant states in porous electromagnetic heat exchangers, J. Appl. Phys. 133 (2023), doi:10.1063/5.0139723.

[19] P.G. Drazin, W.H. Reid, Hydrodynamic Stability, Cambridge University Press, 2004.

[20] K. Chand, M. Sharma, A.K. De, Effect of inclination angle on heat transport properties in two-dimensional Rayleigh–Bénard convection with smooth and rough boundaries, J. Fluid Mech. 950 (2022) A16.

[21] D. Goluskin, C.R. Doering, Bounds for convection between rough boundaries, J. Fluid Mech. 804 (2016) 370–386.

[22] K. Zhong, N. Hutchins, D. Chung, Heat-transfer scaling at moderate Prandtl numbers in the fully rough regime, J. Fluid Mech. 959 (2023) A8.

[23] L.E. Howle, Control of Rayleigh-Bénard convection in a small aspect ratio container, Int. J. Heat Mass Transf. 40 (4) (1997) 817–822.

[24] L.E. Howle, Linear stability analysis of controlled Rayleigh-Bénard convection using shadowgraphic measurement, Phys. Fluids 9 (11) (1997) 3111–3113.

[25] K. Gage, W. Reid, The stability of thermally stratified plane poiseuille flow, J. Fluid Mech. 33 (1) (1968) 21–32.

[26] H.B. Squire, On the stability for three-dimensional disturbances of viscous fluid flow between parallel walls, in: Proceedings of the Royal Society of London. Series A, Containing Papers of a Mathematical and Physical Character, Vol. 142, 1933, pp. 621–628.

[27] J. Gilchrist, G.A. Kriegsmann, D.T. Papageorgiou, Stability of a microwave heated fluid layer, IMA J. Appl. Math. 60 (1) (1998) 73–89.

[28] M. Bhattacharya, T. Basak, Linear stability analysis for the onset of convection during microwave heating of oil confined within horizontal plates, J. Appl. Phys. 105 (2) (2009) 024906.

[29] M. Bhattacharya, T. Basak, Analysis on the onset of microwave induced convection within a horizontal water layer, J. Phys. D Appl. Phys. 41 (15) (2008) 155505.

[30] S. Chandrasekhar, Hydrodynamic and Hydromagnetic Stability, Courier Corporation, 2013.

[31] T.L. Bergman, F.P. Incropera, D.P. DeWitt, A.S. Lavine, Fundamentals of Heat and Mass Transfer, John Wiley & Sons, 2011.

[32] M.N. Sadiku, Numerical Techniques in Electromagnetics with MATLAB, CRC Press, 2011.

[33] J.M. Gaone, B.S. Tilley, V.V. Yakovlev, Permittivity-based control of thermal runaway in a triple-layer laminate, in: IEEE MTT-S Intern. Microwave Symp. Dig. (Honolulu, HI, June 2017), 2017, pp. 459–462.

[34] W. Press, S. Teukolsky, W. Vetterline, B. Flannery, Numerical Recipes: The Art of Scientific Computing, second ed., Cambridge Univ. Press, 1992.